Inorg. Chem. **2007**, *46*, 7767–7781

Inorganic Chemistry
Article

Supramolecular Self-Assembled Polynuclear Complexes from Tritopic, Tetratopic, and Pentatopic Ligands: Structural, Magnetic and Surface Studies

Subrata K. Dey,[†] Tareque S. M. Abedin,[†] Louise N. Dawe,[†] Santokh S. Tandon,[‡] Julie L. Collins,[†] Laurence K. Thompson,*[,†] Andrei V. Postnikov,[§] Mohammad S. Alam,[||] and Paul Müller*[,||]

*Department of Chemistry, Memorial University, St. John's, Newfoundland, A1B 3X7, Canada,
Department of Chemistry, Kent State University, Salem, Ohio 44460, Institute de Physique
Electronique et Chimie Laboratoire de Physique des Milieux Denses, Paul Verlaine University,
1 Bd Arago F-57078, Metz, France, and Physikalisches Institut III, Universität
Erlangen-Nürnberg, Erwin-Rommel-Strasse 1, 91058 Erlangen, Germany*

Received February 21, 2007

Polymetallic, highly organized molecular architectures can be created by "bottom-up" self-assembly methods using ligands with appropriately programmed coordination information. Ligands based on 2,6-picolyldihydrazone (tritopic and pentatopic) and 3,6-pyridazinedihydrazone (tetratopic) cores, with tridentate coordination pockets, are highly specific and lead to the efficient self-assembly of square [3 × 3] Mn_9, [4 × 4] Mn_{16}, and [5 × 5] Mn_{25} nanoscale grids. Subtle changes in the tritopic ligand composition to include bulky end groups can lead to a rectangular 3 × [1 × 3] Mn_9 grid, while changing the central pyridazine to a more sterically demanding pyrazole leads to simple dinuclear copper complexes, despite the potential for binding four metal ions. The creation of all bidentate sites in a tetratopic pyridazine ligand leads to a dramatically different spiral Mn_4 strand. Single-crystal X-ray structural data show metallic connectivity through both μ-O and μ-NN bridges, which leads to dominant intramolecular antiferromagnetic spin exchange in all cases. Surface depositions of the Mn_9, Mn_{16}, and Mn_{25} square grid molecules on graphite (HOPG) have been examined using STM/CITS imagery (scanning tunneling microscopy/current imaging tunneling spectroscopy), where tunneling through the metal d-orbital-based HOMO levels reveals the metal ion positions. CITS imagery of the grids clearly shows the presence of 9, 16, and 25 manganese ions in the expected square grid arrangements, highlighting the importance and power of this technique in establishing the molecular nature of the surface adsorbed species. Nanoscale, electronically functional, polymetallic assemblies of this sort, created by such a bottom-up synthetic approach, constitute important components for advanced molecule-based materials.

Introduction

In the area of "controlled" molecular self-assembly of high nuclearity coordination complexes, ligand design is crucial, and successful approaches with "linear" heterocyclic ditopic, tritopic, and tetratopic pyrimidine- and pyridazine-based ligands have led to the synthesis of a number of square-based polymetallic grids. Examples of M_4 [2 × 2] (Fe(II), Co(II), Zn(II)),[1] M_9 [3 × 3] (Scheme 1; tritopic ligand self-assembly; Ag(I)),[2] and M_{16} [4 × 4] (Pb(II))[3,4] square grids have been reported. A pentatopic pyridazine ligand, synthesized by Lehn did not produce the expected [5 × 5] grid, but instead, an icosanuclear $Ag(I)_{20}$ partial grid formed.[5]

---

* To whom correspondence should be addressed. E-mail: lthomp@mun.ca (L.K.T); phm@physik.uni-erlangen.de (P.M). Fax: 709-737-3702 (L.K.T).
[†] Memorial University.
[‡] Kent State University Salem Campus.
[§] Paul Verlaine University.
[||] Universität Erlangen-Nürnberg.

(1) Patroniak, V.; Baxter, P. N. W.; Lehn, L.-M.; Kubicki, M.; Nissinen, M.; Rissanen, K. *Eur. J. Inorg. Chem.* **2003**, 4001.
(2) Baxter, P. N. W.; Lehn, J.-M.; Fischer, J.; Youinou, M. T. *Angew. Chem., Int. Ed*. **1994**, *33*, 2284.
(3) Garcia, A. M.; Romero-Salguero, F. J.; Bassani, D. M.; Lehn, J-M.; Baum, G.; Fenske, D. *Chem.—Eur. J.* **1999**, *5*, 1803.
(4) Onions, S. T; Frankin, A. M.; Horton, P. N.; Hursthouse, M. B.; Matthews, C. J. *Chem. Commun*. **2003**, 2864.
(5) Baxter, P. N. W.; Lehn, J.-M.; Baum, G.; Fenske, D. *Chem.—Eur. J*. **2000**, *6*, 4510.

10.1021/ic070336a CCC: $37.00

Scheme 1

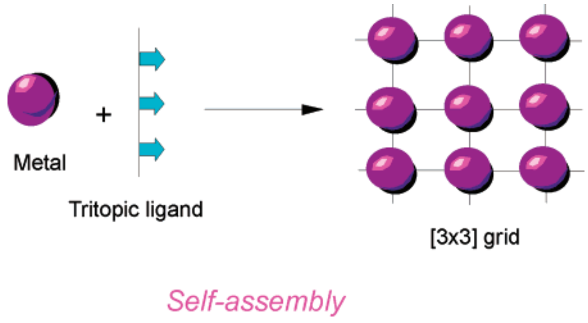

Chart 1

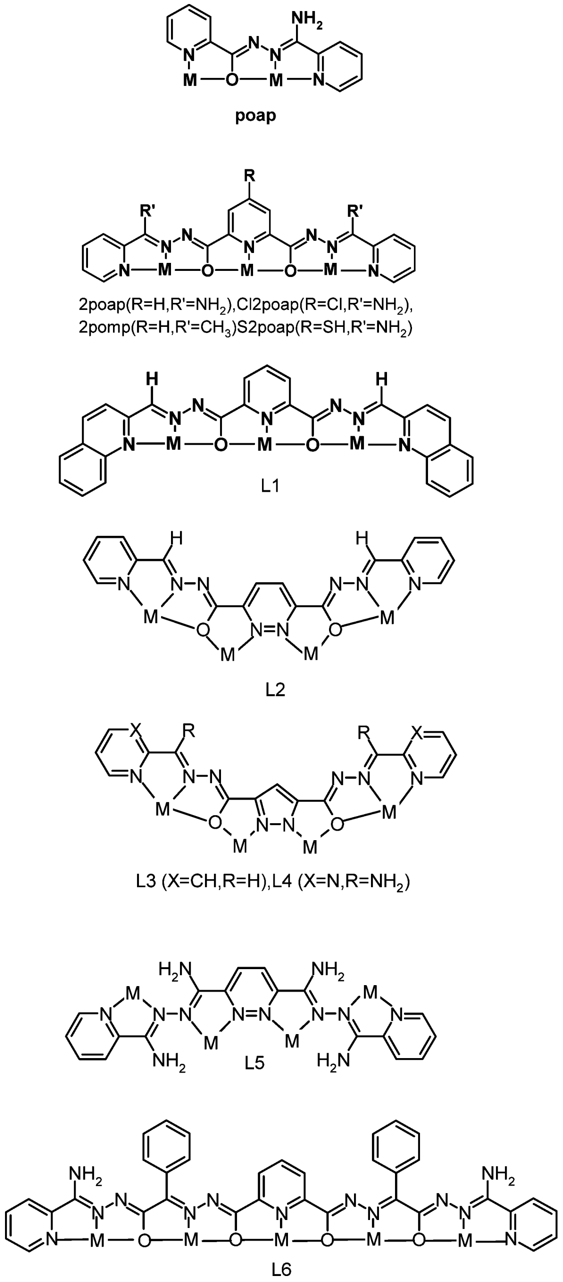

Ligand rotational flexibility, and a preferred *cisoid* conformation, appear to have prevented full [5 × 5] grid assembly.

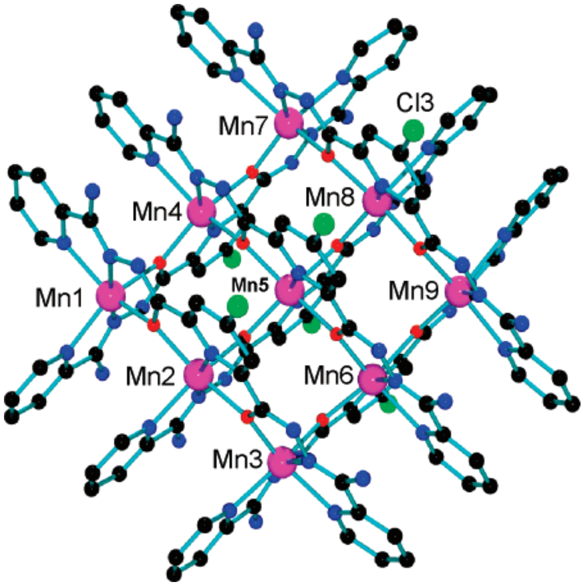

Figure 1. POVRAY structural representaion of the cation in **1**: magenta = Mn, green = Cl, blue = N, red = O, black = C.

Ditopic picolinic hydrazone ligands (e.g., poap, Chart 1) form [2 × 2] self-assembled M_4 square-grid complexes (M = Mn(II), Co(II), Ni(II), Cu(II), Zn(II)) in high yield.[6−8] [3 × 3] M_9 (M = Mn(II), Fe(III), Cu(II), Zn(II)) grids, based on closely related tritopic 2,6-picolinic-dihydrazone ligands (e.g., 2poap and analogues, Chart 1), also form in high yield in the self-assembly reactions (Scheme 1).[9−13] $[Mn_9(Cl2poap)_6](ClO_4)_6$ (**1**)[10] (Figure 1, Chart 1, Cl2poap) is a typical example, with the nine metal ions held in a [3 × 3] grid array within the assembly of six ligands. The Mn(II) centers are antiferromagnetically coupled because of superexchange through the twelve hydrazone oxygen bridges, resulting in a ground-state spin of $S' = 5/2$.

Some $Mn(II)_9$ grids exhibit unprecedented redox properties, with an eight-electron reversible redox window between 0.5 and 1.6 V (vs Ag/AgCl),[9,10,12,13] associated with the oxidation of the eight Mn(II) centers in the outer ring of the grid to Mn(III). The magnetic properties are modulated when oxidation occurs, leading to controlled changes in the ground-state spin.[9,13] Suitably modified grids with sulfur- and

---

(6) Matthews, C. J.; Avery, K.; Xu, Z.; Thompson, L. K.; Zhao, L.; Miller, D. O.; Biradha, K.; Poirier, K.; Zaworotko, M. J.; Wilson, C.; Goeta, A. E.; Howard, J. A. K. *Inorg. Chem.* **1999**, *38*, 5266−5276.

(7) Thompson, L. K.; Matthews, C. J.; Zhao, L.; Xu, Z.; Miller, D. O.; Wilson, C.; Leech, M. A.; Howard, J. A. K.; Heath, S. L.; Whittaker, A. G.; Winpenny, R. E. P. *J. Solid State Chem.* **2001**, *159*, 308.

(8) Dawe, L. N.; Abedin, T. S. M.; Kelly, T. L.; Thompson, L. K.; Miller, D. O.; Zhao, L.; Wilson, C.; Leech, M. A.; Howard, J. A. K. *J. Mater. Chem.* **2006**, 2645.

(9) Zhao, L.; Xu, Z.; Grove, H.; Milway, V. A.; Dawe, L. N.; Abedin, T. S. M.; Thompson, L. K.; Kelly, T. L.; Harvey, R. G.; Miller, D. O.; Weeks, L.; Shapter, J. G.; Pope, K. J. *Inorg. Chem.* **2004**, *43*, 3812.

(10) Thompson, L. K.; Zhao, L.; Xu, Z.; Miller, D. O.; Reiff, W. M. *Inorg. Chem.* **2003**, *42*, 128.

(11) Milway, V. A.; Niel, V.; Abedin, T. S. M.; Xu, Z.; Thompson, L. K.; Grove, H.; Miller, D. O.; Parsons, S. R. *Inorg. Chem.* **2004**, *43*, 1874.

(12) Milway, V. A.; Abedin, T. S. M.; Niel, V.; Kelly, T. L.; Dawe, L. N.; Dey, S. K.; Thompson, D. W.; Miller, D. O.; Alam, M. S.; Müller, P.; Thompson, L. K. *J. Chem. Soc., Dalton Trans.* **2006**, 2835.

(13) Thompson, L. K.; Kelly, T. L.; Dawe, L. N.; Grove, H.; Lemaire, M. T.; Howard, J. A. K.; Spencer, E.; Matthews, C. J.; Onions, S. T.; Coles, S. J.; Horton, P. N.; Hursthouse, M. B.; Light, M. E. *Inorg. Chem.* **2004**, *43*, 7605.

chlorine-appended ligands (Chart 1; e.g., S2poap, Cl2poap; e.g., **1**) adhere to Au(111) surfaces and also form SAMS (self-assembled monolayers), as shown by STM (scanning tunneling microscopy) measurements.[9,14] The flat molecular orientations on the surface are associated with the prominent external positions of the sulfur and chlorine sites on the grid extremities, which provide convenient gold surface-atom contacts. Ordered metallosupramolecular arrays of functionally active molecules of this sort are considered to be important targets for nanoscale device assemblies.[15−18]

Surface studies on **1** deposited on HOPG (highly ordered pyrollytic graphite) have also been carried out and reveal not only the individual grid cations in STM topography but also the spatial arrangement of the individual metal centers using the CITS (current imaging tunneling spectroscopy) technique.[12] This powerful surface structural approach probes the density of states close to the Fermi level of the system, allows discrimination between metal 3d-based HOMO (highest-occupied molecular orbital) levels and ligand orbitals, which occur at quite different energies, and consequently, clearly reveals the metal ion positions. Grid core dimensions obtained by this method closely match those revealed by single-crystal structural methods, even to the details of the canted sideways orientation of the grid on the surface. Similar observations have recently been made with a Co(II)$_4$ [2 × 2] square-grid system,[15] a Cu(II)$_{20}$ wheel-shaped polyanion,[16] and a Fe(III)$_4$ star-shaped cluster.[17] Recent reviews highlight the importance of these techniques for addressing and probing metal centers in supramolecular assemblies applied to surfaces.[18a,b]

The present report describes new manganese and copper complexes of a series of extended polytopic hydrazone ligands and their structural and magnetic properties. Novel extended [4 × 4] and [5 × 5] square Mn(II)$_{16}$ and Mn(II)$_{25}$ grid arrays are discussed, involving tetratopic and pentatopic hydrazone ligands, based on 3,6-pyridazine and 2,6-pyridine cores (Chart 1, L2 and L6). CITS measurements on the new grids clearly reveal the Mn$_{16}$ and Mn$_{25}$ square [n x n] structural motifs. DFT studies on Mn$_9$ are now introduced, showing an exact equivalence with the observed d-orbital MO picture obtained through tunneling experiments.

Experimental Section

Physical Measurements. Infrared spectra were recorded as Nujol mulls using a Mattson Polaris FT-IR instrument, and UV−vis spectra were obtained using a Cary 5E spectrometer. Microanalyses were carried out by Canadian Microanalytical Service, Delta, Canada. Variable-temperature magnetic data (2−300 K) were obtained using a Quantum Design MPMS5S SQUID magnetometer using field strengths in the range of 0.1−5 T. Background corrections for the sample holder assembly and diamagnetic components of the complexes were applied. NMR measurements were taken with a Bruker AVANCE 500 MHz spectrometer. LCMS measurements were taken using an Agilent 1100 Series LC/MSD in APCI mode with methanol and acetonitrile as the solvent.

STM Measurements. All measurements were carried out with a home-built low-drift STM head equipped with commercially available low-current control electronics (RHK technology, with ITHACO preamplifier), under ambient conditions. For high-resolution STM studies, the highly oriented pyrolytic graphite (HOPG) was freshly cleaved. The graphite surface was then imaged by STM to confirm the high resolution of the tip. Mechanically cut Pt−Ir (90/10) tips of diameter 0.25 mm were used. Distances were calibrated in the STM images by observation of the atomic spacing on the HOPG surface. After the graphite surface was successfully imaged, a droplet of the solution in CH_3CN/CH_3OH was deposited (concentration 10^{-9} M) and allowed to run down the graphite surface. Typically, tunneling currents between 5 and 200 pA were employed. The bias voltage was ±100 to ±200 mV. The scan frequency was varied between 2 and 5 Hz. The resolution was 256 × 256 points for topography and 128 × 128 in the CITS measurements. In CITS mode, current−voltage ($I-V$) curves were taken simultaneously with a constant-current STM image with the interrupted-feedback loop technique. The spectroscopic measurements were confined to negative sample-to-tip bias voltages, that is, to the tunneling spectroscopy of occupied molecular energy levels to avoid redox processes.

DFT Calculations. Density functional calculations were performed using the SIESTA method[19] and computer code.[20] Norm-conserving pseudopotentials were generated in the Troullier−Martins scheme[21] and include the states from Mn-3p upward as valence contributors. Atom-centered, strictly confined basis functions (see ref 22 for a detailed discussion on basis functions in SIESTA) were of triple-ζ quality for Mn and double-ζ for other elements. Exchange-correlation was treated in the generalized gradient approximation, according to the formulation by Perdew, Burke, and Ernzerhof.[23] The present results correspond to a single-point calculation using the experimentally determined structure, with the spins of the individual Mn atoms set alternately (i.e., up and down) in the [3 × 3] grid arrangement. The (uncompensated) calculated total magnetic moment of the [3 × 3] grid is 5 μ_B, associated with a spin of $S = 5/2$ at each Mn atom.

Synthesis of Ligands. L1. 2-Quinolinecarboxaldehyde (2.05 g, 1.30×10^{-2} mol) was added to a slurry of pyridine-2,6-dicarbohydrazide (1.29 g, 6.61×10^{-3} mol) in 300 mL of methanol. The resulting mixture was refluxed for 18 h to produce a yellow powder, which was filtered off and washed with diethyl ether to give 2.32 g (4.90×10^{-3} mol, 75% yield) of L1. mp: 230−232 °C. Mass spectrum (m/z APCI+): 474. IR (cm^{-1}): ν_{CO} 1670; ν_{CN} 1554. Anal. Calcd (%) for $C_{27}H_{17}N_7O_2{\cdot}2H_2O$ (bulk sample): C, 61.48; H, 4.74; N, 18.60. Found: C, 61.05; H, 3.85; N, 19.30. This ligand was used without further purification.

---

(14) Shapter, J. G.; Weeks, L.; Thompson, L. K.; Pope, K. J.; Xu, Z.; Johnston, M. R. *Smart Mater. Struct.* **2006**, *15*, S171.

(15) Alam, M. S.; Strömsdörfer, S.; Dremov, V.; Müller, P.; Kortus, J.; Ruben, M.; Lehn, J-M. *Angew. Chem., Int. Ed.* **2005**, *44*, 7896.

(16) Alam, M. S.; Dremov, V.; Müller, P.; Postnikov, A. V.; Mal, S. S.; Hussain, F.; Kortz, U. *Inorg. Chem.* **2006**, *45*, 2866.

(17) Saalfrank, R. W.; Scheurer, A.; Bernt, I.; Heinemann, F. W.; Postnikov, A. V.; Schünemann, V.; Trautwein, A. X.; Alam, M. S.; Rupp, H.; Müller, P. *J. Chem. Soc., Dalton Trans.* **2006**, 2865−2874.

(18) (a) Ruben, M.; Lehn, J.-M.; Müller, P. *Chem. Soc. Rev.* **2006**, *35*, 1056 and references therein. (b) Ruben, M.; Rojo, J.; Romero-Salguero, F. J.; Uppadine, L. H.; Lehn. J.-M. *Angew. Chem., Int. Ed.* **2004**, *43*, 3644 and references therein.

(19) Soler, J. M.; Artacho, E.; Gale, J. D.; García, A.; Junquera, J.; Sánchez-Portal, D.; Ordejón, P. *J. Phys. Condens. Matter* **2002**, *14*, 2745.

(20) http://www.uam.es/siesta.

(21) Troullier, N.; Martins, J. L. *Phys. Rev. B* **1991**, *43*, 1993.

(22) Junquera, J.; Paz, Ó.; Sánchez-Portal, D.; Artacho, E. *Phys. Rev. B* **2001**, *64*, 235111.

(23) Perdew, J. P.; Burke, K.; Ernzerhof, M. *Phys. Rev. Lett.* **1996**, *77*, 3865; (Erratum) *Phys. Rev. Lett.* **1997**, *78*, 1396.

L4. Hydrazine hydrate (1.06 g, 2.12 × 10^{-2} mol) was added to a solution of diethyl 3,5-pyrazoledicarboxylate (1.97 g, 9.28 × 10^{-3} mol) in 175 mL of methanol, and the resulting clear, colorless solution was refluxed for 48 h to produce a white slurry. The white powder (1.54 g, 8.36 × 10^{-3} mol), 1*H*-pyrazole-3,5-dicarbohydrazide, was collected by suction filtration, washed three times with diethyl ether, and added to a neutral solution of methyl pyrimidine-2-carboximidate, produced by the action of sodium in methanol on 1.76 g (1.67 × 10^{-2} mol) of 2-cyanopyrimidine in 200 mL of methanol. A white slurry formed, and the mixture was refluxed for 24 h resulting in the formation of a yellow solid. L4 (3.29 g, 8.34 × 10^{-3} mol, 82% yield overall) was collected by suction filtration and washed three times with diethyl ether. mp: >360 °C. Mass spectrum (*m/z* APCI+): 391.4. IR (cm^{-1}): ν_{NH} 3313; ν_{CO} 1701; ν_{CN} 1631, 1566. Anal. Calcd (%) for $C_{15}H_{14}N_{12}O_2 \cdot 0.5H_2O$ (bulk sample): C, 44.67; H, 3.72; N, 41.69. Found: C, 44.83; H, 3.43; N, 41.95.

L3 was produced in a similar fashion by the reaction of 1*H*-pyrazole-3,5-dicarbohydrazide with pyridine carboxaldehyde and was obtained as a white solid (yield 80%). mp: 239−245 °C. Anal. Calcd (%) for $C_{17}H_{14}N_8O_2 \cdot 2.5CH_3OH$ (bulk sample): C, 52.94; H, 5.32; N, 25.32. Found: C, 53.49; H, 4.51; N, 24.94. **L3** and **L4** were used without further purification.

L6. Methyl benzoyl formate (10.7 g, 65 mmol) was added to 2,6-picolinic acid dihydrazide (6.00 g, 31.0 mmol) suspended in a chloroform/methanol mixture (30/20 mL). The mixture was refluxed overnight, and the volume of the resulting pale yellow solution was reduced, forming the corresponding extended dibenzoyl ester (**2**) as a white powder after 2 days (yield >95%). mp: 190−192 °C. Mass spectrum (*m/z*): 488 (base peak, M + $1)^+$, 428, 368, 282, 222, 105, 77. IR (Nujol, cm^{-1}): ν_{NH} 3326, 3240; ν_{CO} 1743, 1713; ν_{pyr} 999. ^1H NMR (500 MHz, $CDCl_3$): δ 3.91 (s, 6H, OCH_3), 7.45 (m, 6H, Ar−H), 7.79 (d, 4H, Ar−H, J = 7 Hz), 8.18 (t, 1H, Ar−H, J = 8.1 Hz), 8.53 (d, 2H, Ar−H, J = 7.2 Hz), 13.49 (s, 2H, OH).

The extended diester (**2**) (4.0 g, 8.20 mmol) was dissolved in 50 mL of carefully dried THF in a 250 mL three-necked flask under a N_2 atmosphere and cooled in an ice/water bath; 19.0 mL (18.45 mmol) of a 1.0 M solution of hydrazine in THF was added dropwise via syringe, forming a golden yellow solution, which was allowed to slowly come to room temperature and was stirred for 2 days. A pale yellow precipitate of the extended bishydrazone formed, which was filtered off and dried in air (yield 70%). mp: 180−195 °C. Mass spectrum (*m/z*): 488 (M + $1)^+$, 470 (M − H_2O), 342 (base peak). IR (Nujol, cm^{-1}): ν_{NH} 3428, 3316, 3224; $\nu_{CO,CN}$ 1685, 1666, 1619; ν_{py} 998. ^1H NMR (500 MHz, DMSO-d_6): δ δ 3.16 (s, NH_2), 7.50 (s, 6H), 7.73 (t, 4H), 8.24 (m, 3H), 9.94 (s, OH).

The methyl ester of iminopicolinic acid was prepared in situ by reaction of 2-cyanopyridine (0.3 g, 2.88 mmol) with sodium methoxide solution, produced by dissolving sodium metal (0.3 g, 13.0 mmol) in very dry methanol (50 mL) under N_2. The crude extended dihydrazone (0.5 g, 1.0 mmol) was added to the above solution, followed by a few drops of glacial acetic acid to neutralize the excess methoxide. The mixture was stirred at room temperature overnight. A light yellow powder (**L6**) was obtained which was filtered off and air-dried (yield 85%). mp: 228−230 °C. Mass spectrum (APCI, *m/z*): 696 (M + $1)^+$, 678 (M − H_2O), 488, 446 (base peak). IR (cm^{-1}): ν_{NH} 3413, 3324, 3243; ν_{CO} 3158, 1697, 1666; ν_{py} 998. ^1H NMR (500 MHz, DMSO-d_6): δ 6.84 (s, 4H, NH_2), 7.47 (m, 6H, Ar−H), 7.61 (m, 2H, Ar−H), 7.85 (m, 4H, Ar−H), 8.01 (m, 2H, Ar−H), 8.23 (m, 5H, Ar−H), 8.45 (d, 2H, Ar−H, *J* = 4.8 Hz), 9.94 (s, 2H, OH), 11.82 (s, 2H, OH).

Very dry conditions appear to be necessary for the successful synthesis of L6. We have identified the starting bishydrazone, the hydrazone of methyl benzoyl formate, and even the double amidrazone, 2poap (Chart 1), in reactions where dry conditions were not employed.

Synthesis of Complexes. $[Mn_9(L1)_6](ClO_4)_6 \cdot 8H_2O$ (3). L1 (0.12 g, 0.25 mmol) was added to a warm solution of $Mn(ClO_4)_2 \cdot 6H_2O$ (0.14 g, 0.55 mmol) in methanol/acetonitrile (10/10 mL). A cloudy, white suspension formed. The addition of 2 drops of Et_3N produced a dark orange solution, which was stirred for 2 h and kept after filtration for crystallization. Red prismatic crystals, suitable for X-ray analysis, formed after the mixture was left standing for two weeks (yield 0.3 g, 29.5%). Anal. Calcd (%) for $[(C_{27}H_{17}N_7O_2)_6Mn_9](ClO_4)_6 \cdot 8H_2O$ (bulk sample): C, 47.89; H, 2.91; N, 14.89. Found (%): C, 47.87; H, 2.85; N, 14.41.

$[Mn_{16}(L2)_8(OH)_8](NO_3)_8 \cdot 15H_2O$ (4) and $[Mn_{16}(L2)_8(OH)_8](ClO_4)_8 \cdot 15H_2O$ (5). Compound **4** was re-prepared by a slightly different procedure from that described previously.[24] **L2** (0.37 g; 1.0 mmol) was added to a solution of $Mn(NO_3)_2 \cdot 6H_2O$ (0.57 g, 2.0 mmol) in an ethanol/dichloromethane mixture (40/20 mL). Triethylamine (6 drops) was added dropwise, and the mixture was heated for 35 min, with the formation of an orange precipitate. Water (2 mL) was added, resulting in a clear orange solution. Red-orange crystals, suitable for an X-ray structure, formed upon standing (Yield 30%). The structure obtained from this sample represents a significant improvement over that previously reported.

$Mn(ClO_4)_2 \cdot 6H_2O$ (1.45 g, 4.00 mmol) was added as a solid to a stirred white suspension of ligand **L2**[24] (0.75 g, 2.0 mmol) in methanol/acetonitrile (1:1) (30 mL). The addition of a few drops of triethylamine led to the formation of an orange solution, which was stirred for 30 min at ~50 °C and then kept at room temperature. Rectangular orange crystals (**5**) were obtained after two weeks. Anal. calcd (%) for $Mn_{16}(C_{18}H_{12}N_8O_2)_8(OH)_8(ClO_4)_8(H_2O)_{15}$: C, 34.18; H, 2.67; N, 17.72. Found: C, 34.27; H, 2.54; N, 17.42. This sample was used for STS/CITS imagery on HOPG.

$[(L3\text{-}H)Cu_2(OH)(NO_3)(H_2O)](NO_3) \cdot 2H_2O$ (6) and $[(L3\text{-}H)Cu_2(OH)(H_2O)_2](ClO_4)_2 \cdot H_2O$ (7). L3 (0.090 g, 0.25 mmol) was added to a solution of $Cu(NO_3)_2 \cdot 3H_2O$ (0.25 g, 1.0 mmol) in a methanol/water mixture (20/5 mL) and warmed, forming a light green solution. Triethylamine (3 drops) was added with stirring, resulting in the formation of a light blue solid. Five milliliters of water was added, and the mixture was heated with stirring at ~90 °C, forming a bright green solution, which was filtered hot, and the solution was allowed to stand at room temperature. Blue crystals formed after several days, suitable for structural study (yield 0.12 g, 70%). Anal. Calcd (%) for $(C_{17}H_{12}N_8O_2)Cu_2(OH)(NO_3)_2(H_2O)_3$: C, 29.96; H, 2.79; N, 20.56. Found: C, 30.26; H, 2.92; N, 20.56. Compound **7** was synthesized in a similar fashion, using copper perchlorate, and was obtained as blue crystals suitable for structural determination. Anal. Calcd (%) for $(C_{17}H_{12}N_8O_2)Cu_2(OH)(ClO_4)_2(H_2O)_3$: C, 27.02; H, 2.52; N, 14.83. Found: C, 27.04; H, 2.53; N, 14.72.

$[(L4\text{-}H)Cu_2(OH)(H_2O)][(L4\text{-}H)Cu_2(OH)(ClO_4)](ClO_4)_3 \cdot 4H_2O$ (8). L4 (0.12 g, 0.30 mmol) was added to a solution of $Cu(ClO_4)_2 \cdot 6H_2O$ (0.22 g, 0.59 mmol) in methanol/acetonitrile/water (10/20/10 mL) producing a clear, green solution. The addition of 5 drops of Et_3N produced a brown solution, which was stirred and heated gently for 18 h. Upon filtration, a small amount of brown solid was collected and discarded, while the clear green filtrate was kept for crystallization. Blue-green prismatic crystals, suitable for X-ray analysis, formed after the mixture was left standing for 35

---

(24) Dey, S. K.; Thompson, L. K.; Dawe, L. N. *Chem. Commun.* **2006**, 4967.

days (yield 0.05 g, 14%). Anal. Calcd (%) for $(C_{15}H_{12}N_{12}O_2)Cu_2(ClO_4)_2$ (H_2O) (bulk sample): C, 23.97; H, 2.00; N, 22.37. Found (%): C, 24.26; H, 2.03; N, 22.07.

$[(L5)_3Mn_4](ClO_4)_8\cdot 21H_2O$ (9). L5[25] (0.10 g, 0.25 mmol) was added to a solution of $Mn(ClO_4)_2\cdot 6H_2O$ (0.20 g, 0.053 mmol) in methanol/acetronitrile (20/20 mL) with heating and stirring. A clear orange solution formed, which was filtered, reduced in volume, and left to crystallize. Orange crystals of **9** suitable for structural study formed (yield 0.05 g, 20%). Anal. Calcd (%) for $(C_{18}H_{18}N_{12})_3Mn_4(ClO_4)_8(H_2O)_{21}$: C, 24.94; H, 3.72; N, 19.39. Found (%): C, 24.97; H, 2.90; N, 19.20.

[Mn(L6)] (10). A suspension of **L6** (0.10 g, 0.14 mmol) in $MeOH/CHCl_3$ (3:1) was added to a solution of $Mn(CF_3SO_3)_2\cdot xH_2O$ (0.3 g, ~0.8 mmol) in $MeOH/H_2O$ (2:1, 20 mL), and the mixture stirred for 5 h at room temperature. A deep-orange solution formed, which was filtered and kept for crystallization by slow evaporation. A red-yellow polycrystalline solid formed after two weeks (yield 11%). X-ray quality crystals were obtained by slow diffusion of diethyl ether into a solution of the complex in $MeOH/CH_3CN/CHCl_3$ (1:1:1).

$[Mn_{25}(L6)_{10}](ClO_4)_{20}\cdot 65H_2O$ (11). L6 (0.10 g, 0.14 mmol) was added to a solution of $Mn(ClO_4)_2\cdot 6H_2O$ (0.12 g, 0.33 mmol) in ethanol, and the mixture was stirred for 5 h resulting in a dark yellow fine polycrystalline powder (yield 62.5%). IR (Nujol, cm^{-1}): ν_{H_2O} 3548, 3455; ν_{NH} 3355; $\nu_{CO,CN}$ 1646; $\nu_{ClO_4^-}$ 1099 (br). Anal. Calcd (%) for $Mn_{25}(C_{35}H_{27}N_{13}O_4)_{10}(ClO_4)_{20}(H_2O)_{65}$: C, 36.65; H, 3.51; N, 15.87; Cl, 6.18. Found: C, 36.52; H, 2.68; N, 15.45; Cl, 6.29. The addition of a small amount of Et_3N to the powder in a mixture of $CH_3CN/MeOH/CHCl_3$ gave a dark orange solution, from which dark red crystals of **12** were obtained upon addition of ether (yield 50%**)**. This sample was used for STS/CITS imagery on HOPG. Repeated syntheses and recrystallizations of this compound have not yet produced crystals which diffract well enough for a successful structural solution. Solvent inclusions in the crystals appear to cause significant mosaic spread.

X-ray Crystallography. A light blue prism crystal of **8** having approximate dimensions of 0.36 × 0.17 × 0.14 mm was mounted on a glass fiber. All measurements were made on a Rigaku Saturn CCD area detector diffractometer with graphite-monochromated Mo Kα radiation. The data were collected at a temperature of -160 ± 1 °C to a maximum 2θ value of 62.5°. Of the 21 786 reflections that were collected, 9766 were unique ($R_{int} = 0.0789$); equivalent reflections were merged. Data were collected and processed using CrystalClear (Rigaku).[26] The structure was solved by direct methods[27] and expanded using Fourier techniques.[28] Some non-hydrogen atoms were refined anisotropically, while the rest were refined isotropically. Hydrogen atoms were refined using the riding model.

Neutral atom scattering factors were taken from Cromer and Waber.[29] Anomalous dispersion effects were included in F_{calcd};[30] the values for $\Delta f'$ and $\Delta f''$ were those of Creagh and McAuley.[31] The values for the mass attenuation coefficients are those of Creagh and Hubbell.[32] All calculations were performed using the CrystalStructure[33,34] crystallographic software package, except for refinement, which was performed using SHELXL-97.[35]

Diffraction intensities for **3**−**7**, **9**, **10**, and **L5** were collected similarly, and structural solutions were achieved using the same methods (see Table 1 and Supporting Information). For **3**, the Platon[36] Squeeze procedure was applied to recover 396.7 electrons per unit cell in four voids (3203.8 Å^3), that is, 99.2 electrons per asymmetric unit. Disordered solvent water and acetonitrile molecules appeared to be present prior to the application of Squeeze, although a good point atom model could not be achieved. The application of Squeeze gave a good improvement in the data statistics. For **9**, apparent twinning effects were dealt with using Rigaku's Twin Solve[26] software to generate a single-component reflection data file, which was then treated normally.

Results and Discussion

Structural Studies. $[Mn_9(L1)_6](ClO_4)_6\cdot 8H_2O$ (3). The full and core cationic structures of **3** are shown in Figure 2, and important bond distances and angles are listed in Table 2. The self-assembled grid has a remarkable rectangular structure, representing the first example in this class. Six ligands encompass nine Mn(II) ions with three in a μ-O bridging conformation and three in a μ-NN bridging conformation. The "NN" bridging ligands span the long rectangle dimensions, linking the Mn3−Mn6−Mn9, Mn2−Mn5−Mn8, and Mn1−Mn4−Mn7 metal groupings and are arranged on the same side of the rectangle in a roughly parallel fashion. The "O" bridging ligands span the short dimensions (Mn1−Mn2−Mn3, Mn4−Mn5−Mn6, Mn7−Mn8−Mn9), but the end ligands project on one side of the rectangle, while the central ligand projects on the other side. The normal Mn_9 square grids have all μ-O bridges, but the μ-NN mode has been observed before in octanuclear Cu_8 complexes with related ligands.[37,38] The short Mn−Mn (μ-O) distances fall in the range of 4.142−4.182 Å, while the longer Mn−Mn (μ-NN) distances fall in the range of 5.216−5.616 Å. These distances are consistent with the bridge group sizes. Mn−O−Mn angles fall in the range of 132.2−134.4 °, and the Mn−N−N−Mn torsional angles fall in the range of 160.6−179.1 °. These large μ-O and μ-NN bridge angles are

---

(25) Matthews, C. J.; Onions, S. T.; Morata, G.; Davis, L. J.; Heath, S. L.; Price, D. J. *Angew. Chem.* **2003**, *42*, 3166.

(26) (a) *CrystalClear*; Rigaku Corporation: The Woodlands, TX, 1999. (b) *CrystalClear Software User's Guide*; Molecular Structure Corporation: The Woodlands, TX, 2000. (c) Pflugrath, J. W. *Acta Crystallogr.* **1999**, *D55*, 1718−1725.

(27) Sheldrick, G. M. *SHELX97*; University of Göttingen: Göttingen, Germany, 1997.

(28) Beurskens, P. T.; Admiraal, G.; Beurskens, G.; Bosman, W. P.; de Gelder, R.; Israel, R.; Smits, J. M. M. *The DIRDIF-99 Program System*; Technical Report of the Crystallography Laboratory; University of Nijmegen: Nijmegen: The Netherlands, 1999.

(29) Cromer, D. T.; Waber, J. T. *International Tables for X-ray Crystallography*, Vol. IV; The Kynoch Press: Birmingham, U.K., 1974; Table 2.2A.

(30) Ibers, J. A.; Hamilton, W. C. *Acta Crystallogr.* **1964**, *17*, 781.

(31) Creagh, D. C.; McAuley, W. J. *International Tables for Crystallography*, Vol. C; Wilson, A. J. C., Ed.; Kluwer Academic Publishers: Boston, 1992; Table 4.2.6.8, pp 219−222.

(32) Creagh, D. C.; Hubbell, J. H. *International Tables for Crystallography*, Vol. C; Wilson, A. J. C., Ed.; Kluwer Academic Publishers: Boston, 1992; Table 4.2.4.3, pp 200−206.

(33) *CrystalStructure 3.7.0*: *Crystal Structure Analysis Package*; Rigaku and Rigaku/MSC: The Woodlands, TX, 2000−2005.

(34) Watkin, D. J.; Prout, C. K.; Carruthers, J. R.; Betteridge, P. W. *CRYSTALS*, issue 10; Chemical Crystallography Laboratory: Oxford, U.K., 1996.

(35) Sheldrick, G. M. *SHELX97*; University of Göttingen: Göttingen, Germany, 1997.

(36) Spek, A. L. *J. Appl. Crystallogr.* **2003**, *36*, 7−13.

(37) Milway, V. A.; Niel, V.; Abedin, T. S. M.; Xu, Z.; Thompson, L. K.; Grove, H.; Miller, D. O.; Parsons, S. R. *Inorg. Chem.* **2004**, *43*, 1874.

(38) Milway, V. A.; Abedin, T. S. M.; Thompson, L. K.; Miller, D. O. *Inorg. Chim. Acta* **2006**, *359*, 2700.

Table 1. Summary of Crystallographic Data for **3**, **4**, **6**−**9**, and **L5**

	3	**4**	**6**	**7**
empirical formula	$C_{162}H_{102}N_{42}Mn_9O_{36}Cl_6$	$C_{144}H_{134}N_{72}O_{63}Mn_{16}$	$C_{17}H_{20}N_{10}O_{12}Cu_2$	$C_{17}H_{23.6}N_8O_{15.8}Cl_2Cu_2$
M	3920.01	4760.1	683.51	790.82
cryst syst	monoclinic	orthorhombic	monoclinic	monoclinic
space group	$P2_1/n$	I_{222}	$C2/c$	$P2_1$
a (Å)	20.908(4)	13.27(2)	25.238(3)	8.1242(5)
b (Å)	27.102(4)	21.36(3)	13.5859(16)	20.8794(14)
c (Å)	32.492(5)	33.87(5)	14.2647(17)	8.3519(6)
α (deg)				
β (deg)	98.239(4)		93.864(3)	103.6728(12)
γ (deg)				
V (Å^3)	18222(5)	9603(26)	4880.9(10)	1376.57(16)
ρ_{calcd} (g cm^{-3})	1.429	1.646	1.860	1.908
T (K)	153(1)	153(1)	153(1)	153(1)
Z	4	2	8	2
μ (cm^{-1})	7.72	11.14	18.28	18.30
reflns collected				
total	137 797	19 686	22 308	13 809
unique	37 263	8536	5617	7058
R_{int}	0.0513	0.051	0.036	0.0242
obsd ($I > 2.00\sigma(I)$)	37 263	8536	5617	7058
2θ range (deg)	0−55.00	0−51.00	0−55.00	0−61.50
params	2297	677	372	435
final R1, wR2^a	0.0936, 0.2597	0.1229,0.3768	0.0524,0.1429	0.0362,0.0961

	8	**9**	**10**	**L5**
empirical formula	$C_{15}H_{16.6}N_{12}Cu_2O_{12.8}Cl_2$	$C_{66}H_{73}N_{42}O_{32.5}Mn_4Cl_8$	$C_{35}H_{27}N_{13}O_4Mn$	$C_{18}H_{18}N_{12}$
M	767.77	2478.02	748.62	402.4
cryst syst	triclinic	monoclinic	monoclinic	monoclinic
space group	P	$C2/c$	Cc	$P2_1/n$
a (Å)	12.180(6)	14.508(2)	15.140(10)	7.0375(9)
b (Å)	14.450(6)	19.241(3)	10.791(7)	27.752(4)
c (Å)	16.120(7)	36.547(5)	21.138(13)	9.9941(14)
α (deg)	68.36(5)			
β (deg)	77.37(4)	90.801(9)	97.04(2)	97.328(4)
γ (deg)	75.81(5)			
V (Å^3)	2530.7(20)	10201(3)	3427(4)	1936.0(4)
ρ_{calcd} (g cm^{-3})	2.015	1.614	1.451	1.381
T (K)	113(2)	153(1)	153(1)	153(1)
Z	4	4	4	4
μ (cm^{-1})	19.83	7.91	4.462	0.94
reflns collected				
total	21 786	13 026	14 455	17 298
unique	9766	8731	6893	4398
R_{int}	0.0789	0.049	0.050	0.0227
obsd ($I > 2.00\sigma(I)$)	9766	8731	6893	4398
2θ range (deg)	0−52.00	0−52.00	0−61.50	0−55.00
params	829	713	486	272
final R1, wR2^a	0.1203, 0.3187	0.0918,0.2390	0.0883,0.2174	0.0453,0.1210

[a] R1 = $\sum 2F_0{*} - {*}F_c2/\sum {*}F_0{*}$, wR2 = $[\sum[w({*}F_0{*}^2 - {*}F_c{*}^2)^2]/\sum[w({*}F_0{*}^2)^2]]^{1/2}$.

suggestive of intramolecular antiferromagnetic exchange (vide infra).[9−13,39]

One of the molecular features, which appears to characterize the [3 × 3] square grids in general, is the facility with which the ligands align themselves in the two roughly parallel groups of three above and below the grid metal pseudoplane (see Figure 1). Separation between the ligands in this case is 4 Å or less, suggesting that π interactions between the aromatic rings are important. The slight offset between adjacent parallel pyridine aromatic rings indicates the normal tendency of such rings to minimize π repulsions. The quinoline end pieces on **L1** are clearly much larger aromatic components than the pyridine rings normally present in this ligand type, and it is reasonable to assume that, as the ligands approach each other in the typical grid arrangement, the π interactions are considerably greater. In the N−N bridging mode, the metal ions will, of necessity, be further apart and, by default, will then allow the π-rich ligand end pieces to get further apart, thus creating the opportunity for the formation of a rectangle rather than a square.

$[Mn_{16}(L2)_8(OH)_8](NO_3)_8\cdot 15H_2O$ (4). The structure of the hexadecanuclear cation in **4** is shown in Figure 3a, and a labeled core structural representation is shown in Figure 3b. Important bond distances and angles are listed in Table 3. A brief report of an essentially identical structure appeared recently but with a different space group.[24] However, in the present structure, all the required nitrate anions were located, which was not possible previously. Consequently, more complete structural details are now considered. The overall grid structure is really a composite of four [2 × 2] $[Mn_4(\mu\text{-}O)_4]$ corner grid subunits with hydrazone oxygen bridges, connected in the center by a combination of eight pyridazine

---

(39) Xu, Z.; Thompson, L. K.; Miller, D. O.; Clase, H. J.; Howard, J. A. K.; Goeta, A. E. *Inorg. Chem.* **1998**, *37*, 3620 and references therein.

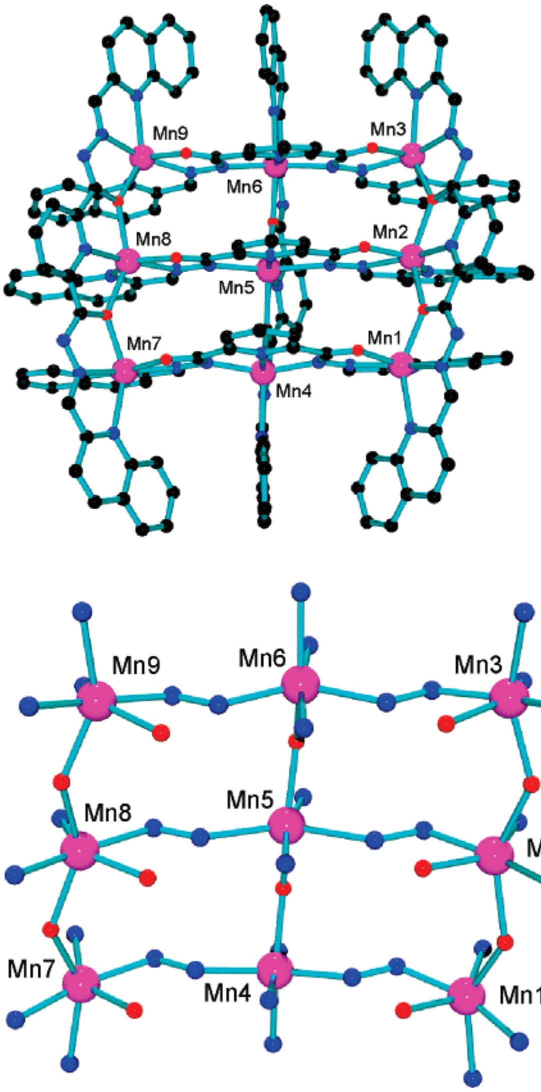

Figure 2. POVRAY structural representations of the cation in **3**: magenta = Mn, blue = N, red = O, black = C.

Table 2. Bond Distances (Å) and Angles (deg) for **3**

Mn1	N2	2.135(5)	Mn5	O3	2.272(3)
Mn1	N37	2.167(4)	Mn5	N33	2.373(4)
Mn1	N36	2.228(5)	Mn5	N31	2.441(4)
Mn1	O1	2.228(3)	Mn6	N13	2.134(4)
Mn1	O11	2.231(4)	Mn6	N25	2.184(4)
Mn1	N1	2.441(4)	Mn6	N26	2.200(4)
Mn2	O9	2.147(4)	Mn6	N24	2.253(4)
Mn2	N4	2.162(4)	Mn6	O4	2.262(3)
Mn2	N30	2.259(4)	Mn6	N14	2.378(4)
Mn2	N29	2.262(4)	Mn7	N16	2.126(5)
Mn2	O1	2.304(3)	Mn7	N41	2.165(4)
Mn2	O2	2.327(3)	Mn7	O5	2.221(4)
Mn3	N6	2.136(4)	Mn7	O12	2.227(4)
Mn3	N23	2.178(4)	Mn7	N42	2.259(5)
Mn3	O7	2.187(4)	Mn7	N15	2.397(5)
Mn3	O2	2.242(4)	Mn8	O10	2.156(3)
Mn3	N22	2.248(4)	Mn8	N18	2.184(4)
Mn3	N7	2.417(4)	Mn8	N35	2.254(4)
Mn4	N9	2.124(4)	Mn8	N34	2.257(4)
Mn4	N39	2.185(4)	Mn8	O6	2.283(3)
Mn4	N38	2.200(4)	Mn8	O5	2.321(4)
Mn4	N40	2.208(4)	Mn9	N20	2.142(5)
Mn4	O3	2.244(3)	Mn9	N27	2.161(4)
Mn4	N8	2.435(4)	Mn9	O8	2.224(4)
Mn5	N11	2.176(4)	Mn9	O6	2.240(4)
Mn5	N32	2.200(4)	Mn9	N28	2.258(5)
Mn5	O4	2.266(3)	Mn9	N21	2.449(4)
Mn1	O1	Mn2	134.37(18)		
Mn3	O2	Mn2	132.49(16)		
Mn4	O3	Mn5	133.30(15)		
Mn6	O4	Mn5	132.33(15)		
Mn7	O5	Mn8	133.11(16)		
Mn9	O6	Mn8	133.56(15)		

(N−N) and eight hydroxide (μ-OH) bridges. The ligands are essentially flat and have a *cis* conformation, which ensures that the metals all bind on one side of each ligand. This, combined with the formation of five-membered chelate rings throughout, ensures that the ligand components are aligned appropriately for efficient grid self-assembly.

Hydrazone Mn−O−Mn bridge angles fall in the range of 119−129°, while the Mn−OH−Mn angles fall in the range of 118−127°. Mn−Mn distances for pyridazine-bridged metal pairs fall in the range of 3.6−3.7 Å, while Mn−Mn distances for those pairs bridged by hydrazone oxygen atoms fall in the range of 3.8−4.0 Å, more typical of the [2 × 2] and [3 × 3] Mn grids.[8−10,12,13] The grid has a roughly flat, square overall molecular footprint with edge lengths of ~21 Å (2.1 nm). However, closer examination of the core (Figure 3c) reveals that the metals are far from coplanar and that there is considerable puckering of the metallic core itself. This would be expected on the basis of the projected natural bend in **L2** (Chart 1), which would not occur in ligands based on a central 2,6-picolinic hydrazone core. A preliminary X-ray structural study on **5** indicates the same cationic fragment as in **4**.

[(L3-H)Cu_2(OH)(NO_3)(H_2O)](NO_3)·2H_2O (6). The structure of **6** is shown in Figure 4, and important distances and angle are listed in Table 4. Surprisingly, the structure consists of a dinuclear cation, with the two copper ions bridged by the central pyrazole group, and the incorporation of a second, adventitious hydroxide bridge. The ligand adopts an unusual *cis* conformation, in which the hydazone oxygen and diazine NN groups are not involved in bridging, and the ligand end pieces form a tridentate N_3 coordinating pocket, with a mixture of five- and six-membered chelate rings. The net result is a near perfect fit of the metal ions in the pockets forming an almost planar dinuclear entity. The Cu−Cu separation is 3.282 Å, and the Cu−OH−Cu angle 117.9 °. The two copper ions are square pyramidal, with an axial nitrate bound to Cu(1) and an axial water molecule bound to Cu(2). The fortuitous arrangement of these two groups allows a hydrogen-bonding connection between O(10) and nitrate O(4), which may help to stabilize the Cu_2 subunit (*vide infra*). The O(4)−O(10) distance is 2.812 Å, and the O−H−O angle 169.8 °.

[(L3-H)Cu_2(OH)(H_2O)$_2$](ClO_4)$_2$·H_2O (7). The structural representation of the dinuclear cation in **7** is shown in Figure 5, and important bond distances and angles are listed in Table 5. The structure is very similar to that of **6**, with two water molecules in a *trans* arrangement occupying axial positions at the square pyramidal copper centers. The Cu−Cu distance is 3.308 Å, and the Cu−OH−Cu angle 117.5 °. The absence of any intramolecular hydrogen bonding interaction, present

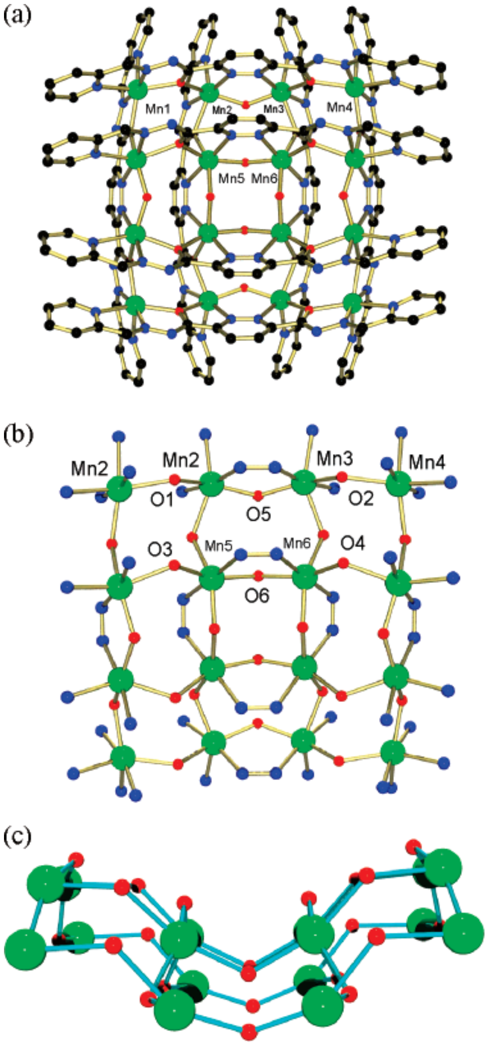

Figure 3. POVRAY structural representations of the cation in **4**: green = Mn, blue = N, red = O, black = C.

Table 3. Bond Distances (Å) and Angles (deg) for **4**

Mn1	N2	2.102(10)	Mn4	N7	2.161(10)
Mn1	N2	2.102(10)	Mn4	N7	2.161(10)
Mn1	O1	2.164(8)	Mn4	O2	2.196(8)
Mn1	O1	2.164(8)	Mn4	O2	2.196(8)
Mn1	N1	2.295(9)	Mn4	N8	2.316(11)
Mn1	N1	2.295(9)	Mn4	N8	2.316(11)
Mn2	O5	2.032(8)	Mn5	O6	2.061(10)
Mn2	O1	2.194(9)	Mn5	O6	2.061(10)
Mn2	N10	2.203(10)	Mn5	O3	2.194(8)
Mn2	O3	2.232(8)	Mn5	O3	2.194(8)
Mn2	N4	2.255(11)	Mn5	N12	2.302(9)
Mn2	N9	2.261(9)	Mn5	N12	2.302(9)
Mn3	O5	2.022(8)	Mn6	O6	2.047(10)
Mn3	N15	2.166(11)	Mn6	O6	2.047(10)
Mn3	O4	2.222(8)	Mn6	O4	2.184(8)
Mn3	O2	2.223(9)	Mn6	O4	2.184(8)
Mn3	N5	2.233(11)	Mn6	N13	2.288(9)
Mn3	N16	2.260(12)	Mn6	N13	2.288(9)

Mn1	O1	Mn2	126.1(4)
Mn4	O2	Mn3	126.1(4)
Mn5	O3	Mn2	120.5(3)
Mn6	O4	Mn3	121.9(4)
Mn3	O5	Mn2	128.3(4)
Mn6	O6	Mn5	123.7(7)

in **6**, indicates the inherent stability of the dinuclear unit and the apparently preferred dinucleating ligand bonding mode.

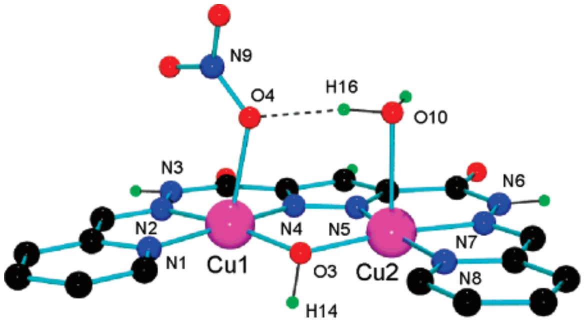

Figure 4. POVRAY structural representation of the cation in **6**.

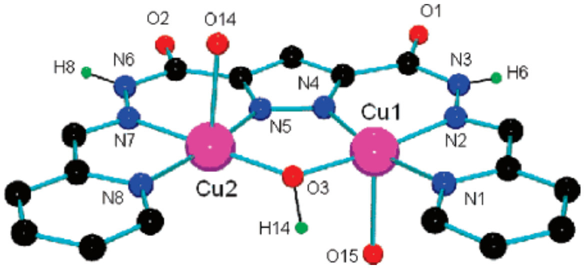

Figure 5. POVRAY structural representation of the cation in **7**.

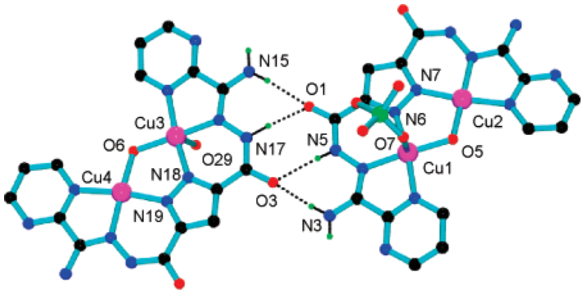

Figure 6. POVRAY structural representation of the cations in **8**.

Table 4. Bond Distances (Å) and Angles (deg) for **6**

Cu1	O3	1.927(2)	Cu2	N5	1.933(2)
Cu1	N4	1.935(3)	Cu2	O3	1.942(2)
Cu1	N1	1.990(3)	Cu2	N8	1.978(2)
Cu1	N2	2.035(3)	Cu2	N7	2.042(2)
Cu1	O15	2.368(2)			
Cu1	O3	Cu2	117.52(10)		

Table 5. Bond Distances (Å) and Angles (deg) for **7**

Cu1	O3	1.927(2)	Cu2	N5	1.933(2)
Cu1	N4	1.935(3)	Cu2	O3	1.942(2)
Cu1	N1	1.990(3)	Cu2	N8	1.978(2)
Cu1	N2	2.035(3)	Cu2	N7	2.042(2)
Cu1	O15	2.368(2)			
Cu1	O3	Cu2	117.52(10)		

[(L4-H)Cu_2(OH)(H_2O)][(L4-H)Cu_2(OH)(ClO_4)](ClO_4)$_3$·4H_2O (8). The structure of **8** is shown in Figure 6, and important bond distances and angles are listed in Table 6. Compound **8** has a structure similar to that of **6** and **7**, but with two slightly different hydroxo-bridged dinuclear copper complex ions in the asymmetric unit. In one, a water molecule (O(29)) is bonded to Cu(3), while in the other a perchlorate is bonded via O(7) to Cu(1), creating a combination of square and square pyramidal centers in both subunits. Cu−Cu distances are 3.244 Å (Cu(1)−Cu(2)) and 3.254 Å (Cu(2)−Cu(3)), with corresponding Cu−OH−Cu angles of

Table 6. Bond Distances (Å) and Angles (deg) for **8**

Cu1	O5	1.903(7)	Cu3	N18	1.911(8)
Cu1	N6	1.918(8)	Cu3	N13	1.954(8)
Cu1	N1	1.947(8)	Cu3	N16	1.969(8)
Cu1	N4	1.963(8)	Cu3	O29	2.292(8)
Cu1	O7	2.263(8)	Cu4	O6	1.903(7)
Cu2	O5	1.883(7)	Cu4	N19	1.923(8)
Cu2	N7	1.922(8)	Cu4	N24	1.951(8)
Cu2	N12	1.950(8)	Cu4	N21	1.956(8)
Cu2	N9	1.960(9)	Cu4	O18	2.420(9)
Cu3	O6	1.879(7)			

Cu2	O5	Cu1	117.9(3)
Cu3	O6	Cu4	118.7(3)

Table 7. Bond Distances (Å) and Angles (deg) for **L5**

N1	C5	1.3397(17)	N7	C11	1.3322(16)
N1	C1	1.3436(18)	N8	C12	1.3453(16)
N2	C6	1.3425(17)	N9	C12	1.3054(16)
N3	C6	1.2946(17)	N9	N10	1.4070(14)
N3	N4	1.4105(14)	N10	C13	1.2978(16)
N4	C7	1.2985(17)	N11	C13	1.3488(16)
N5	C7	1.3491(16)	N12	C14	1.3345(17)
N6	C8	1.3360(16)	N12	C18	1.3402(18)
N6	N7	1.3379(15)			

C5	N1	C1	117.17(12)
C6	N3	N4	113.73(10)
C7	N4	N3	109.00(10)
C8	N6	N7	119.39(10)
C11	N7	N6	120.39(10)
C12	N9	N10	110.78(10)
C13	N10	N9	111.92(10)
C14	N12	C18	117.78(12)

117.9 and 118.7 ° respectively. One novel and fascinating feature of the structure of **8** surrounds the well-matched docking of the two dinuclear subunits via a concerted hydrogen-bonding network involving the external O−N−N groups. N−O distances fall in the range of 2.765−2.886 Å, with four such connections between each dinuclear center. Figure 6 just shows the association between Cu(1) and Cu(3), but it extends via similar connections between Cu(2) and Cu(4) and creates a flat bifurcated extended chain of Cu_2 subunits. A molecular view of a segment of this extended structure is shown in Figure S1 (see Supporting Information). Interestingly, this extended hydrogen-bonded structure is reminiscent of the cytosine−guanine base-pair interaction in DNA.

L5 and [(L5)$_3$Mn$_4$](ClO$_4$)$_8$·21H$_2$O (9). The structure of ligand **L5** is shown in Figure 7, and some distances and angles are listed in Table 7. Protons were located on N(2), N(5), N(8), and N(11) from difference maps, indicating that the ligand exists in a tautomeric form in which all the diazine CN bonds have essentially double bond character (1.295−1.305 Å). The ligand adopts a *trans* arrangement at its ends with respect to the NH_2 groups, with C−N−N−C torsional angles of 154.9 and 168.3°, indicating a slight out-of-plane rotation about the N−N bonds.

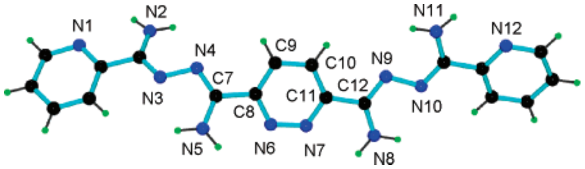

Figure 7. POVRAY structural representation of the ligand **L5**.

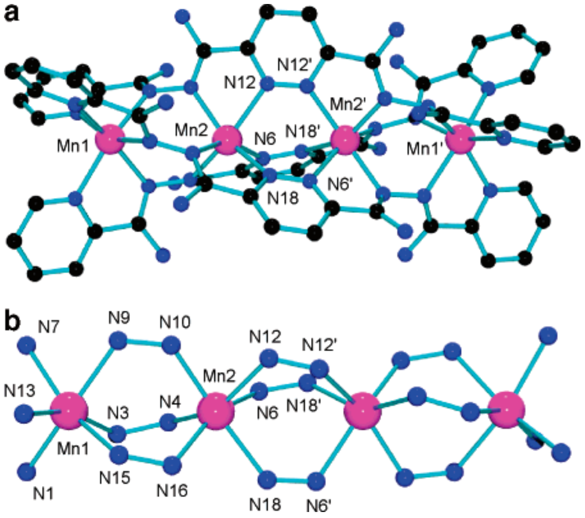

Figure 8. POVRAY structural representations of the cation in **9**.

Table 8. Bond Distances (Å) and Angles (deg) for **9**

Mn1	N15	2.216(5)	Mn2	Mn2′	3.850(3)
Mn1	N9	2.226(5)	Mn2	N10	2.155(5)
Mn1	N1	2.228(5)	Mn2	N16	2.158(5)
Mn1	N7	2.230(6)	Mn2	N4	2.190(5)
Mn1	N13	2.235(6)	Mn2	N6	2.237(5)
Mn1	N3	2.243(5)	Mn2	N12	2.256(5)
Mn1	Mn2	3.802(3)	Mn2	N18	2.256(5)

Mn1	N15	N16	Mn2	31.9
Mn1	N3	N4	Mn2	26.9
Mn1	N9	N10	Mn2	34.1
Mn2	N6	N18′	Mn2′	21.7
Mn2	N12	N12′	Mn2′	32.9

Table 9. Bond Distances (Å) and Angles (deg) for **10**

Mn1	N11	2.129(6)	Mn1	O3	2.158(4)
Mn1	O4	2.144(6)	Mn1	N1	2.298(6)
Mn1	N3	2.146(6)	Mn1	N13	2.385(6)

N11	Mn1	O4	107.3(2)
N11	Mn1	N3	159.16(19)
O4	Mn1	N3	72.8(2)
N11	Mn1	O3	73.06(19)
O4	Mn1	O3	90.68(19)
N3	Mn1	O3	127.56(19)
N11	Mn1	N1	112.2(2)
O4	Mn1	N1	140.3(2)
N3	Mn1	N1	71.8(2)
O3	Mn1	N1	96.8(2)
N11	Mn1	N13	70.30(19)
O4	Mn1	N13	93.1(2)
N3	Mn1	N13	88.85(19)
O3	Mn1	N13	142.59(19)
N1	Mn1	N13	103.6(2)

The structure of the tetranuclear cation in **9** is shown in Figure 8a, and a core structure is shown in Figure 8b. Important distances and angles are listed in Table 8. This complex has an unusual linear spiral structure with four six-coordinate Mn(II) ions encompassed by three ligands, which all have a pronounced twist, and bridge the metal centers by open-chain diazine and pyridazine NN groups. Mn−Mn distances along the chain are 3.802 Å (Mn(1)−Mn(2)), involving the open chain diazine bridge, and 3.850 Å, involving the pyridazine bridge. The twisting about the NN bridges can be quantified via the Mn−N−N−Mn torsional angles which fall in the range of 26.9−34.1 ° for Mn(1) and Mn(2) and 21.7−32.9 ° for Mn(2) and Mn(2)′. These are of

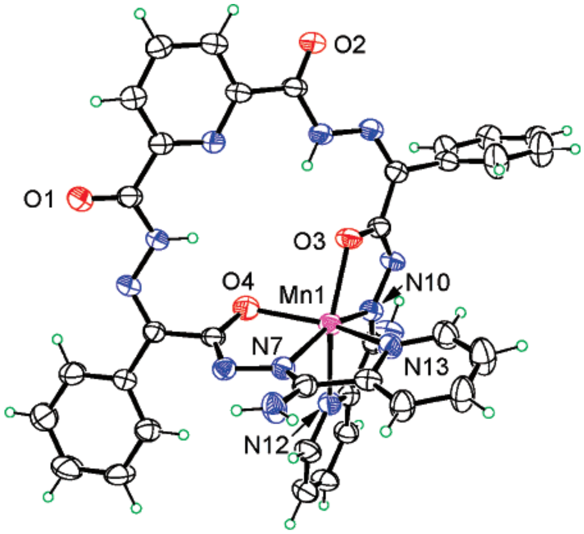

Figure 9. ORTEP structural representation of the complex **10**.

relevance for the magnetic exchange analysis (vide infra). There appears to be only one other related tetranuclear example of a spiral chain of this sort with Cu(II) and the same ligand.[25] However, smaller dinuclear spiral complexes with the simpler, closely related ligand PAHAP (picolinamide azine) and Mn(II), Fe(II), Co(III), and Ni(II) are well documented.[39] These involve just open-chain diazine bridges.

[Mn(L6)] (10). The ligand **L6** has the appropriate design elements to bind five metals in its five coordination pockets in a roughly linear fashion (Chart 1), as a result of the contiguous linear arrangement of ten potentially five-membered chelate rings. It is therefore encoded with the coordination information necessary to possibly generate a [5 × 5] grid upon self-assembly with a six-coordinate metal ion. Reactions of **L6** with Mn(II) salts produced orange crystalline solids (see experimental), but in the case of Mn(CF_3SO_3)$_2$, the mononuclear complex **10** was obtained in low yield. The structure reveals a simple neutral mononuclear complex (Figure 9), with the manganese ion bonded to two deprotonated ligand end pockets, which bend around and encompass the metal creating a *cis*-N_4O_2 pseudo-octahedral coordination sphere. Important distances and angles are listed in Table 9. Mn−N distances fall in the range of 2.129−2.385 Å, and the Mn−O distances are 2.144 and 2.158 Å.

Oligomeric species have been observed with tritopic picolinic hydrazone ligands, although not frequently,[10,40] and indicate clearly that while the [$n \times n$] grids are favored thermodynamically, other polynuclear and mononuclear species are also possible and appear to depend in part on the metal ion present. In the case of Mn(II) complexes of **L6**, significant difficulties have been experienced with poor crystal diffraction, and despite other positive evidence for full grid formation, no structural solution has been forthcoming. However indirect structural evidence through surface studies on **12** does show a [5 × 5] grid formation (vide infra).

Surface Studies and DFT Calculations. The use of single molecules in a device capacity requires that they can be probed and appropriately activated via some suitable molecular property. Fixing their positional location can be achieved by application to a surface, with a monolayer assembly as a reasonable goal. The [3 × 3] Mn grids have been applied to both Au(III) and HOPG surfaces and imaged using STM and CITS techniques.[9,12,14] The power of CITS imagery rests not only with the ability to actually tunnel current through an individual molecule but also with the ability to tunnel though individual metal atoms with appropriate tuning of tunneling energies.[12] This probes exclusively the metal d HOMO states, thus creating an image of the surface-applied grid molecule based on its metal ion components only. STM and CITS images of **1** adsorbed on HOPG are shown in Figure 10a and b, respectively.[12]

To substantiate the role of the metal 3d HOMO states in the CITS imagery, first-principle calculations of the electronic structure of the Mn_9 grid **1** have now been carried out using density functional theory (DFT).[19−23] Figure S2 (Supporting Information) shows the spin-resolved local density of states of the Mn atoms at three different sites (Mn1 corner, Mn2 side, Mn5 center). The DFT calculations demonstrate that the HOMOs are constructed from the 3d-states of Mn(II) and that the energy gap between the HOMO and the LUMO is 0.44 eV. It follows that the molecular orbitals within an energy window between the Fermi level (E_F) and −0.9 eV would give a significant contribution exclusively from the 3d states of the Mn1, Mn2, and Mn5 centers. Therefore, no noticeable positional contrast would be expected for the oxygen and nitrogen atoms. This is consistent with the CITS data (Figure 10b), which means that the highest peak of the density of states is located at 0.9 eV below the Fermi level, and so maximum contrast in the measurements would be expected at bias voltages below −0.9 V. On the basis of the calculated energies, decreasing the bias voltage from zero, the corner Mn atoms should contribute to the signal first, followed by the central Mn and then the side Mn atoms. This is indeed observed in the STS experiments (Figure 10c). Also no significant O- and N-related states are observed down to −0.9 V, which is also in good agreement with DFT calculations. A 3D representation of the calculated electron density map summing up all occupied states down to −0.9 eV is shown in Figure 10d. The experimental observation at −0.879 V (Figure 10e) is quite consistent with the predicted DFT data

Mn_{16} and Mn_{25}. STM measurements on **5** (Mn_{16}) applied as a dilute solution to a freshly cleaved HOPG surface show that the molecules self-organize into well-ordered arrays along the monatomic step edges of the HOPG surface (Figure 11a−b). Simultaneously recorded STM topography and CITS current images on a singly deposited molecule are shown in Figure 11c and d, respectively. STM topography (11c) shows a featureless blob with an outer diameter of approximately 2.8 nm, which is roughly consistent with the dimensions of a single molecular cation, as determined from the X-ray crystallographic data. The CITS technique is again capable of selectively probing the manganese HOMO 3d states at

---

[40] Kelly, T. L.; Milway, V. A.; Grove, H.; Niel, V.; Abedin, T. S. M.; Thompson, L. K.; Zhao, L.; Harvey, R. G.; Miller, D. O.; Leech. M.; Goeta, A. E.; Howard, J. A. K. *Polyhedron* **2005**, *24*, 807.

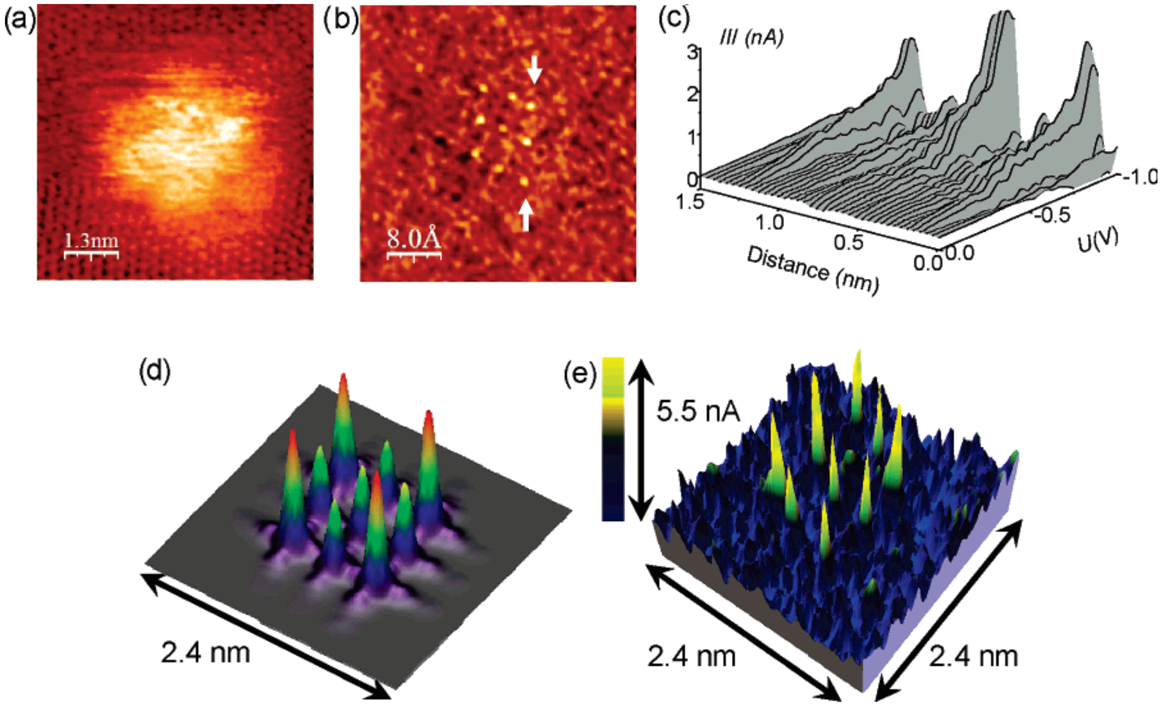

Figure 10. STM/CITS images of Mn [3 × 3] grid complex **1** deposited onto a HOPG surface. (a) STM image showing the underlying HOPG lattice and an isolated Mn complex simultaneously ($V = 100$ mV, $I = 50$ pA). (b) CITS current image at bias voltage −0.879 V. The grid structure appears to be slightly distorted because of thermal drift of the scanning piezo tip. (c) 3D representation of a set of $I-V$ characteristics recorded at 38 equidistant positions between the two arrows in Figure 10b. (d) 3D representation of DFT-calculated electron density maps within an energy window between E_F and −0.9 eV. (e) FFT filtered view of Figure 10b on an enlarged scale, measured at −0.879 V. The 3D picture is rotated to match the DFT-calculated image (Figure 10d).

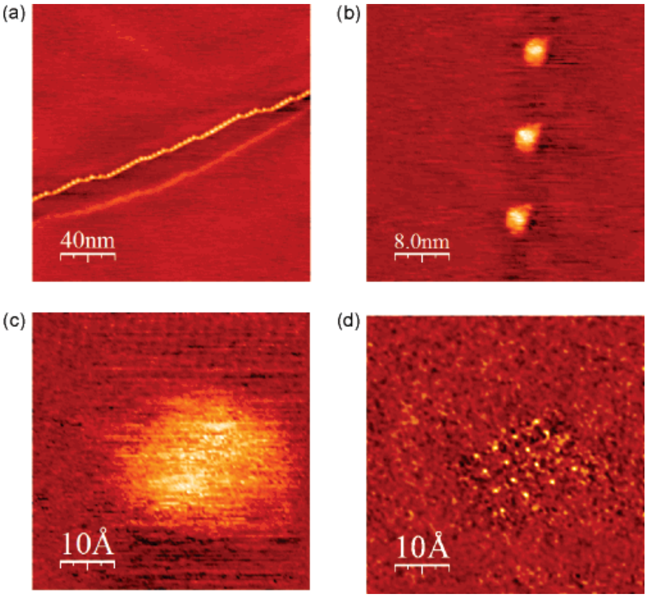

Figure 11. STM/CITS images of the Mn_{16} [4 × 4] complex **5** on an HOPG substrate representing (a) a large-scale STM image ($V = 100$ mV, $I = 5$ pA); (b) isolated single molecules, under the same imaging conditions as in panel a; (c) constant current STM topography; and (d) CITS current image of the same area at a bias of −0.4 V recorded simultaneously with topography. Figure 11d is averaged two times using Gaussian smoothing to increase the signal-to-noise ratio.

negative sample bias, and Figure 11d reveals a group of image spots in a gridlike arrangement, which clearly correspond to the sixteen Mn(II) centers. Estimated distances of separation are entirely consistent with those observed in X-ray crystallography. Close inspection of the image indicates that the metal sites are in a nonlinear puckered arrangement, again in direct agreement with the X-ray structural results.

The putative Mn_{25} grid sample **12** was deposited on HOPG from a very dilute solution in CH_3CN/MeOH and examined using STM/CITS experiments. Figure 12a shows the STM topography of a single molecular line arranged on an HOPG surface, with the molecules residing predominantly at the step edges of the HOPG surface. Figure 12b shows a high-resolution STM image of a single complex ion, with background regions of the frame showing atomic resolution of the HOPG substrate. The roughly square-shaped feature has an outer diameter of approximately 3.2 nm, close to the expected diameter of 2.8 nm of a single Mn_{25} grid molecule, based on a simple extension of the molecular dimensions of known Mn_9 and Mn_{16} grids. CITS spectroscopy was also performed, and the topography of a single molecule (Figure 12c) mapped simultaneously with CITS again shows a rather featureless entity. Estimates of its size are ∼2.8 × 3.2 Å, consistent with the expected dimensions of a Mn_{25} grid.

CITS measurements were carried out at ramping voltages comparable to those used for the Mn_9 and Mn_{16} grids. Remarkably, the metal atomic positions are clearly revealed in a regular [5 × 5] gridlike array (Figure 12d). The estimated metallic grid core dimensions from this image give a square with an edge length of ∼17 Å (1.7 nm), in complete agreement with Mn−Mn separations in the Mn_4, Mn_9, and Mn_{16} grids, with hydrazone oxygen bridging connections, which are close to 4 Å. A segment of the $Mn(II)_{25}$ grid showing just the middle row of metal centers is illustrated in relief form in Figure 13, by plotting current isopols as a function of voltage. The 3D peaks represent the metal ion

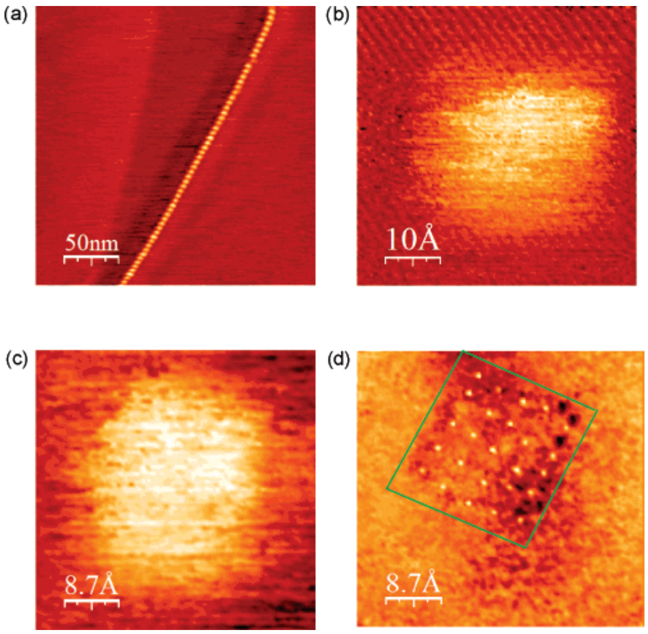

Figure 12. STM/CITS measurements of putative Mn [5 × 5] complex showing (a) constant current topography of a linear chain of single molecules ($I = 5$ pA, $V = 100$ mV); (b) an isolated single molecule with atomic scale resolution of HOPG ($I = 50$ pA and $V = 200$ mV); and (c and d) simultaneously recorded constant current topography and CITS current image recorded at −0.732 V. The topographic parameters were 100 mV and 30 pA. Figure 12d is averaged with the same procedure used in Figure 11d.

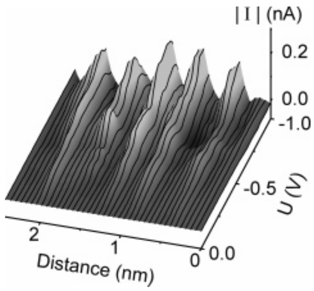

Figure 13. 3D representation of a set of $I-V$ characteristics recorded at 39 equidistant positions along the middle row of peaks of a CITS map of the Mn [5 × 5]. The background current, arising from the HOPG substrate, has been subtracted. Five peaks are clearly visible. The average distance between neighboring peaks is 0.4 nm.

positions, with the expected Mn−Mn peak−peak separations of ~0.4 nm. This remarkable result confirms the fact that there are twenty five metals in the grid core, separated by distances consistent with the expected hydrazone oxygen bridges, but absolute proof of the presence of the expected ten ligands has not been obtained directly, since with the experimental CITS conditions chosen, only the metal ion electronic states are probed. However, it is reasonable to assume that such an arrangement exists, based on the elemental analytical data, and because it is highly unlikely that all the metals would be seen in this expected grid arrangement without the organizing effect of the ligands.

Magnetic Properties. Variable-temperature magnetic data for **3** are shown in Figure 14, with a drop in moment (per mole) from 17.7 μ_B at 300 K to 6.4 μ_B at 2 K. This is consistent with the presence of nine Mn(II) centers within an antiferromagnetically coupled grid. Dealing with a full matrix calculation on this 45-electron problem from first principles is not possible because of the immensity of the matrix calculations involved. Even the application of point-group symmetry-reduction methods would still involve an enormous calculation.[41,42] Because the rectangular grid comprises three $[M_3\text{-}(\mu\text{-}O)_2]$ subunits separated by μ-NN bridges, an approximate data fit was approached by considering **3** as a composite of three linear trinuclear subunits. The total spin quantum number combinations and their energies for the appropriate exchange Hamiltonian ($H_{ex} = -J\{S_1S_2 + S_2S_3\}$) were calculated and substituted into the van Vleck equation (eq 1) within the software package MAGMUN4.11,[43] to give a reasonable data fit. The solid line in Figure 14 was obtained in a best fit analysis for $g = 2.01$, $J = -2.32$ cm^{-1}, TIP = 0 cm^3 mol^{-1}, $\rho = 0.007$, and $\theta = -3.6$ K ($10^2R = 4.9$; $R = [\sum(\chi_{obsd} - \chi_{calcd})^2/\sum\chi_{obsd}{}^2]^{1/2}$; ρ = fraction of paramagnetic impurity, TIP = temperature-independent paramagnetism, θ = Weiss correction), with magnetic data scaled for Mn(II)$_3$ subunits. The J value is consistent with related square Mn(II)$_9$ grids with μ-O bridges. The substantial negative θ value can be interpreted in terms of an antiferromagnetic exchange interaction between the Mn$_3$ subunits.

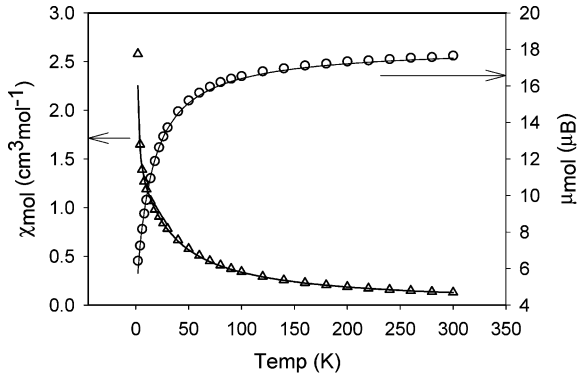

Figure 14. Variable-temperature magnetic data for **3** (see text for fitted parameters).

$$\chi_M = \frac{N\beta^2g^2}{3k(T-\theta)}\frac{\sum S'(S'+1)(2S'+1)e^{-E(S')/kT}}{\sum(2S'+1)e^{-E(S')/kT}}(1-\rho) + \frac{N\beta^2g^2S(S+1)\rho}{3kT} + \text{TIP} \quad (1)$$

The variable-temperature magnetic data for **4** and **5** are essentially identical and show a moment at 300 K of ~22 μ_B consistent with the presence of sixteen Mn(II) ions (5.5 μ_B per metal), dropping to ~4 μ_B at 2 K, indicating significant intramolecular antiferromagnetic exchange. The profile for **4** is shown in Figure 15. Once again, the

---

[41] Waldmann, O.; Güdel, H. U.; Kelly, T. L.; Thompson, L. K. *Inorg. Chem.* **2006**, *45*, 3295.

[42] Thompson, L. K.; Waldmann, O.; Xu, Z. *Coord. Chem. Revs.* **2005**, *249*, 2677.

[43] MAGMUN4.11/OW01.exe is available as a combined package free of charge from the authors (http://www.ucs.mun.ca/~lthomp/magmun). MAGMUN was developed by Dr. Zhiqiang Xu (Memorial University), and OW01.exe was developed by Dr. O. Waldmann. We do not distribute the source codes. The programs may be used only for scientific purposes, and economic utilization is not allowed. If either routine is used to obtain scientific results, which are published, the origin of the programs should be quoted.

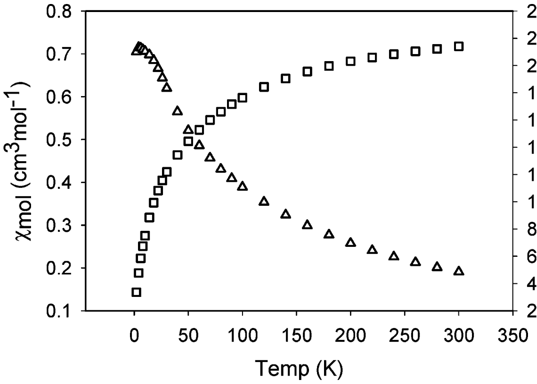

Figure 15. Variable-temperature magnetic data for **4**.

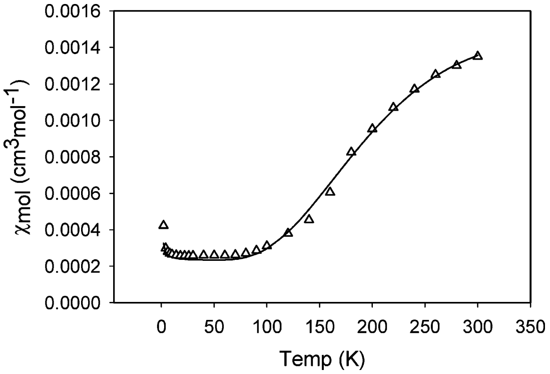

Figure 16. Variable-temperature magnetic data for **6** (see text for fitted parameters).

magnitude of the spin-state matrix calculation prevents any direct assessment of the exchange picture in this system. In keeping with the J values for **3** and other related Mn(II) [2 × 2] and [3 × 3] grids (e.g., **1**) with comparable Mn−O−Mn angles, exchange integrals of -2 to -5 cm^{-1} would be expected.[7,9,10,24] A ground state spin of $S' = 0$ would be anticipated for this even-numbered metal grid, but magnetization versus field data at 2 K (Figure S3) indicate significant residual spin, consistent with the nonzero moment at this temperature.

Variable-temperature magnetic data for **6** are shown in Figure 16, with susceptibility rising to a maximum above 300 K, consistent with intramolecular antiferromagnetic exchange between the two copper centers via both the pyrazole and OH bridges. The data were fitted to a simple dinuclear exchange expression ($H_{ex} = -J\{S_1S_2\}$ within MAGMU4.11 to give $g = 2.26(2)$, $J = -443(4)$ cm^{-1}, TIP $= 230 \times 10^{-6}$ cm^3 mol^{-1}, $\rho = 0.0002$, and $10^2R = 1.8$ (eq 1). The solid line in Figure 16 was calculated with these parameters. Pyrazole bridges have been shown to propagate antiferromagnetic exchange. A bis-μ-pyrazolato-bridged dicopper(II) complex with trigonal-bipyramidal metal geometries was shown to have $J = -188$ cm^{-1},[44] while in other bis-μ-pyrazolato-bridged dicopper(II) complexes involving square pyramidal geometries, larger J values (-330, -426 cm^{-1}) were observed.[45] The bridge combination in **6** involves pyrazole and hydroxide, and the large Cu−OH−Cu bridge angle (117.9 °) suggests that hydroxide would provide a significant if not dominant contribution to the total exhange. It is of interest to note that in a series of related dinuclear copper(II) complexes with equivalent combinations of pyridazine or phthalazine and hydroxide bridges, a magnetostructural correlation indicates an exchange integral of $-J = \sim 580$ cm^{-1} for this OH bridge angle.[46] These combinations appear therefore to be more effective at propagating antiferromagnetic exchange than the present pyrazole/OH combination. Compound **7** has an almost identical magnetic profile, and fitting to the same exchange Hamiltonian gave $g = 2.11(2)$, $J = -398(5)$ cm^{-1}, TIP $= 195 \times 10^{-6}$ cm^3 mol^{-1}, $\rho = 0.014$ ($10^2R = 1.3$). The J value is consistent with the double bridge, and the large Cu−OH−Cu bridge angle (117.5 °).

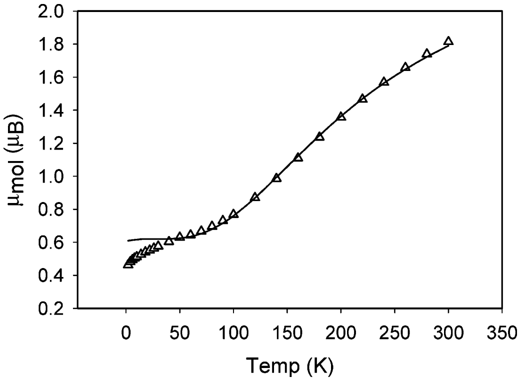

Figure 17. Variable-temperature magnetic data for **8** (see text for fitted parameters).

Compound **8** has a similar magnetic profile in general to that of **6** and **7**, with moment per mole dropping from 1.81 μ_B at 300 K to 0.46 μ_B at 2 K, indicating substantial residual spin in what is clearly a strongly coupled dinuclear copper(II) system (Figure 17). Data treatment using a simple dinuclear model ($H_{ex} = -J\{S_1S_2\}$) did not produce a very good fit below 120 K, and the best fit gave $g = 2.02(4)$, $J = -357(12)$ cm^{-1}, TIP $= 100 \times 10^{-6}$ cm^3 mol^{-1}, $\rho = 0.05$, and $\theta = -3.8$ K ($10^2R = 3.8$). The J value is consistent with **6** and **7**, but a low g value prompted us to examine an alternate exchange model in which the hydrogen-bonded chain structure of **8** is considered to possibly contribute to the overall exchange process. An alternating chain model[47,48] was therefore tested ($H_{ex} = -\mathbf{2}[J\{S_iS_{i+1}\} + \alpha J\{S_{i+1}S_{i+2}\}]$) and found to give a significant improvement in fitting, particularly in the lower-temperature regime. The solid line in Figure 17 is calculated for $g = 2.07$, $J = -187$ cm^{-1}, $\theta = -4$ K, $\rho = 0.04$, $\alpha = 0.2$, and TIP $= 50 \times 10^{-6}$ cm^3 mol^{-1} ($10^2R = 1.6$). Varying α above and below this value led to significantly worse fits. While this cannot be considered a rigorous approach to the exchange model for **8**, particularly given the large number of fitted parameters and the poor fit below 40 K, the improvement of the fitting with the alternating chain equation is significant. It suggests that

---

(44) Tanase, S.; Koval, I. A.; Bouwman, E.; de Gelder, R.; Reedijk, J. *Inorg. Chem.* **2005**, *44*, 7860.

(45) de Geest, D. J.; Noble, A.; Moubaraki, B.; Murray. K. S.; Larsen, D. S.; Brooker, S. *Dalton Trans.* **2007**, 467.

(46) Thompson, L. K.; Lee, F. L.; Gabe, E. J. *Inorg. Chem.* **1988**, *27*, 39.

(47) Duffy, W.; Barr, K. P. *Phys. Rev.* **1968**, *165*, 647.

(48) Hall, J. W.; Marsh, W. E.; Weller, R. R.; Hatfield, W. E. *Inorg. Chem.* **1981**, *20*, 1033.

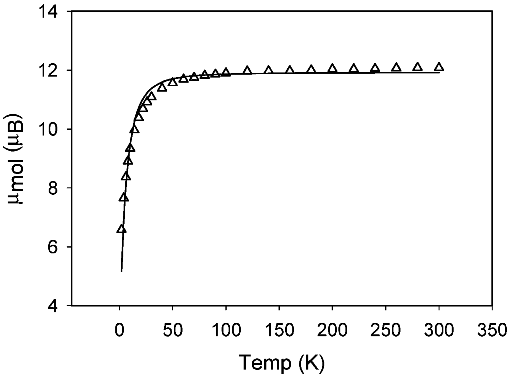

Figure 18. Variable-temperature magnetic data for **9** (see text for fitted parameters).

the extended hydrogen-bonded structure is influencing the overall exchange and provides a conduit for weak magnetic communication between the dinuclear centers.

Variable-temperature magnetic data for the Mn_4 strand **9** (Figure 18) show a moment per mole dropping from 12.1 μ_B at 300 K to 6.5 μ_B at 2 K, indicating overall dominant intramolecular antiferromagnetic exchange. Each pair of external adjacent Mn(II) ions is bridged by three open-chain diazine groups in a twisted spiral arrangement, while the inner pair is bridged by three twisted pyridazine NN groups. It is constructive, to assess the possible magnetic nature of the bridging interactions, to compare **9** with the closely related complex $[Mn_2(pahap)_3](ClO_4)_4$,[39] which has a spiral arrangement of three equivalent open-chain diazine bridges linking two Mn(II) centers. Mn−N−N−Mn torsion angles in this compound are 44.2° on average and lead to weak intramolecular ferromagnetic exchange ($2J = 2.1$ cm^{-1}, $H_{ex} = -2J\{S_1S_2\}$). The average Mn−N−N−Mn angle for **9** is 31.0 °. Such a small angle would reasonably lead to a ferromagnetic exchange term as well.[39] Given the general trend of antiferromagnetic exchange in pyridazine-bridged dicopper,[49,50] dimanganese, and other dimetal systems,[51] an antiferromagnetic exchange term would reasonably be anticipated for the central triple pyridazine bridge in **9**. With these considerations in mind, the fitting for **9** was approached using the exchange Hamiltonian $H_{ex} = -J_1\{S_1S_2 + S_3S_4\} - J_2\{S_2S_3\}$, but limitations were set on J_1 and J_2 to avoid possibly “overfitting” the data in a free-form regression. Preliminary fitting was carried out using a range of J_1/J_2 ratios, and the range which appeared to approach the best fit region was $J_1/J_2 = -0.5$. A basis set of theoretical S'/energy data for all spin vector couplings in the model were then calculated assuming $J_1/J_2 = -0.5$, and the experimental data fitted accordingly using MAGMUN4.11. A close fit gave $g = 2.015(10)$, $J_1 = +1.6(1)$ cm^{-1}, $J_2 = -3.2(1)$ cm^{-1}, and TIP = 0 cm^3 mol^{-1}. The solid line in Figure 18 was calculated using these parameters. The fitted J_1 value is consistent with previously reported open-chain diazine spirally bridged systems. The closely related Cu_4 spiral chain complex $[Cu_4(L5)_3](ClO_4)_8$[25] shows a very slight drop in moment from 280 to 5 K, associated with a possible combination of ferromagnetic and antiferromagnetic exchange terms, but no analysis of the exchange situation was carried out.

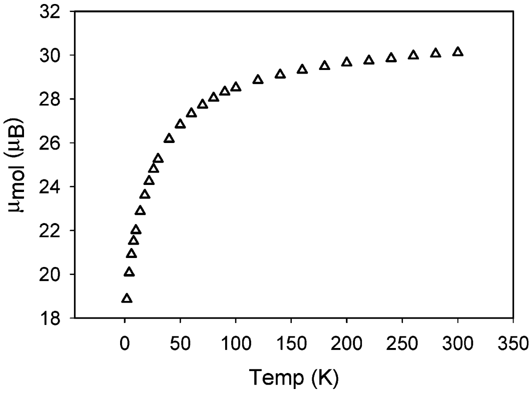

Figure 19. Variable-temperature magnetic data for **12**.

Magnetic data on complexes **11** and **12** show room-temperature moments of ~30 μ_B, consistent with the presence of 25 Mn(II) centers ($\mu_{SO} = 29.6$ μ_B), dropping to ~ 19 μ_B at 2 K, again indicating the presence of intramolecular antiferromagnetic exchange (see Figure 19 for data on **12)**. A comparison of both **11** and **12** with the well-understood $Mn(II)_9$ [3 × 3] grids[8−12] might suggest that the ground state for the Mn_{25} grid would approach $S' = 5/2$, because of the presence of an odd number of spin centers, and the expected presence of an interconnected [5 × 5] grid network of Mn(II) ions, with putative μ-O-type bridging linkages. The moments at 2 K for are much higher than expected and suggest that the exchange coupling situation is different from that apparent in the lower-order antiferromagnetic [$n \times n$] Mn(II) grids, and perhaps weaker than expected. Magnetization data for **12**, measured as a function of field at 2 K (see Supporting Information Figure S3), show a rise to very large Nβ values as field increases, approaching 55 Nβ at 5 T, consistent with a large number of residual spins in the grid at this temperature. The M/H profile shows no saturation and is best interpreted in terms of a large collection of $S = 5/2$ spin subunits in the grid, with weak overall antiferromagnetic exchange. This in itself is most interesting, given the confined space within which such a large pool of electrons (125) would reside. Efforts are underway to understand more thoroughly the nature of the spin coupling in these highly electron-rich nanometer scale grids and to obtain direct structural information through X-ray crystallography for $Mn(II)_{25}$.

Conclusions

Linear polytopic hydrazone ligands with coordination pockets connected by small flexible bridges (e.g., O, N−N) self-assemble in the presence of metal ions to give square and rectangular grids and also chains. The grids clearly have a high degree of thermodynamic stability, since other smaller oligomeric entities are uncommon, although in the case of a

---

(49) Mandal, S. K.; Thompson, L. K.; Gabe, E. J.; Charland, J-P.; Lee, F. L. *Inorg. Chem.* **1988**, *27*, 855.

(50) Thompson, L. K.; Mandal, S. K.; Charland, J-P.; Gabe, E. J. *Can. J. Chem.* **1988**, *66*, 348.

(51) Lan, Y.; Kennepohl, D. K.; Moubaraki, B.; Murray, K. S.; Cashion, J. D.; Jameson, G. B.; Brooker, S. *Chem. Eur. J.* **2003**, *9*, 3772.

(52) Horcas, I.; Fernandez, R.; Gomez-Rodriguez, J. M.; Colchero, J.; Gomez-Herrero, J.; Baro, A. M. *Rev. Sci. Instrum.* **2007**, *78*, 013705.

tetratopic pyrazole ligand, copper prefers to form dinuclear complexes. The short bridging connections between metal ions encourage intramolecular spin exchange and electronic communication between the metal centers. Examples of both antiferromagnetic and ferromagnetic exchange have been discussed, with ferromagnetic coupling between Mn(II) centers resulting from an acute twist of the metal−ligand bonds around the N−N diazine bridges.

Surface imaging techniques (STM/CITS) show the core metallic nature of the individual Mn_{25} grid cations, with 25 manganese centers showing up clearly, disposed at the expected distances of separation in a [5 × 5] square grid arrangement, despite the absence of a crystal structure. This is based convincingly on structurally documented [3 × 3] and [4 × 4] examples, and their CITS measurements. It also highlights the novel and potentially important use of this new structural probe, which, while not establishing the complete structural features of a complex ion, determines the nuclearity, and the metal ion core arrangement.

The ability to apply these grid molecules to surfaces and to probe the molecules and individual metal atoms using tunneling techniques sets the stage for the possible use of this type of nanoscale molecular entity in a device context. The rich electrochemistry and redox "bistability"[12] observed with the $Mn(II)_9$ grids, in which controlled and reversible redox changes occur, could allow an individual molecule to store binary information, under the simple influence of an applied electrical potential, and the selective probing of individual metal atoms within the grid using the CITS technique suggests that "multistability" within a single molecule may also be possible. This, coupled with the formation of a monolayer assembly of such a system on a suitable surface, could lead to the ultraminiaturization of information storage subunits by a bottom-up molecular construction technique, rather than a top-down approach, which is currently used. This could then lead to the creation of very high density information storage media. Studies to further examine and exploit these systems are ongoing.

Acknowledgment. We thank the Natural Sciences and Engineering Research Council of Canada (L.K.T.) and SFB 583, Deutsche Forschungsgemeinschaft (P.M.), for funding to support these studies. Figures 10−12 were generated using the program WSxM [Nanotec Electrónica, Madrid].[52]

Supporting Information Available: Crystallographic data in CIF format and figures showing extended structural features of **8**, the local density if states at three Mn sites in **3**, magnetization versus field data for **4**, and magnetization versus field data for **12**. This material is available free of charge via the Internet at http://pubs.acs.org.

IC070336A